scientific reports

OPEN

Inclined bending seismic reflection layer in the crust illuminated by distributed fibre-optic-sensing measurements in western Japan

Masatoshi Miyazawa

Distributed acoustic sensing (DAS), which enables a single fibre-optic cable to function as multiple sensors, is a technique to measure the strain rate distributed along the cable. This technique is applied to record ground motions in western Japan via a 50 km-long fibre-optic cable beneath a national road. The measured values are strain changes along the cable every 5 m, corresponding to 9788 sensor deployments. This high-density measurement along the long cable successfully recorded the 2021 M2.8 and M3.2 earthquakes that occurred in the crust within the distance of the cable in southern Kyoto. The direct S waves were followed by seismic waves approximately 8–14 s later, which were reflected by lower crustal structures. These waveforms were previously reported by observing many earthquakes via multiple seismometers, but the DAS observations clearly illuminate reflected wavefields from single earthquake observations for the first time. The numerical simulation of the strain-rate wavefields of these earthquakes reveals the existence of a north-dipping thin layer with a slow seismic velocity in the lower crust, which becomes steeper in the shallower part. This layer might represent the path of slab-derived fluid to the shallow fault zone.

Compared with conventional seismometers that need to be installed individually, distributed fibre optic sensing techniques are new, powerful tools in seismology[1]. In general, the distributed acoustic sensing (DAS) interrogator continuously emits signals with a laser wavelength of 1550 nm into a fibre-optic cable and receives Rayleigh backscattered signals due to impurities to measure the phase changes for a gauge at any given location along the cable. The phase changes can be directly converted to strain rates, corresponding to the time derivative of the strain measured for the gauge along the cable direction. The advantages include high-density measurements of ground motion along tens of kilometres of fibre at few-metre intervals at a high sampling rate. Previous studies have reported offshore and onshore observations of regional earthquakes[2–5] and remote earthquakes[6–8]. These acquired data have also been applied to investigate seismic structures in the crust[9]. On the other hand, compared with conventional earthquake observations, fewer earthquake observations are available via DAS because of its novelty and limited application.

In southern Kyoto in western Japan, the background seismicity in the crust is high, and the 2018 Mw 5.6 Osaka earthquake occurred nearby[10,11] (Fig. 1). In this region, the National Route 9 runs in a NW-SE direction, and the fibre-optic cable is installed beneath this route and managed by the Kyoto Road office. Thus, DAS measurements taken by this fibre-optic cable should reveal earthquakes at thousands of stations, increasing the number of earthquake observations by DAS. Moreover, the existence of an inclined seismic reflector in the lower crust has been reported[12–14] via seismic migration methods. The reflector may be related to the occurrence of low-frequency earthquakes, even apart from volcanoes and plate boundaries, where these types of earthquakes are often observed. S waves from earthquakes that occur around southern Kyoto are often followed by reflected waves, which are S waves when the travel time and dominance of horizontal components are considered. These observations are evidence of seismic reflectors. For example, from observations of seismic signals approximately 10 s after direct S waves, the existence of north-dipping reflectors in the lower crust was inferred[12]. More seismic data, including those taken at campaign seismic stations, were used to show the three-dimensional structure of the reflector, which reached the depth of low-frequency earthquakes from approximately 30–35 km[13]. Furthermore, the structure images were improved by considering the inclined reflector structure; however, the continuity of reflectors is still unclear[14], and the characteristics of the physical quantities of reflectors were not provided. An

Disaster Prevention Research Institute, Kyoto University, Uji, Kyoto 611-0011, Japan. email: miyazawa.masatoshi.5z@kyoto-u.ac.jp

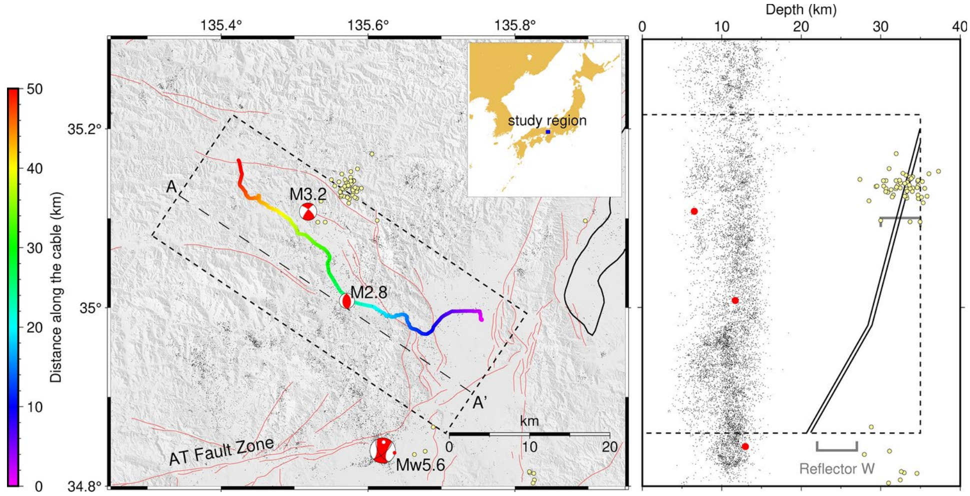

Fig. 1. Fibre-optic geometry and seismicity in southern Kyoto, Japan. The distance along the cable is measured from the Kyoto Road office. The focal mechanisms of the M2.8 and M3.2 earthquakes observed by DAS are shown. The mechanism of the 2018 Mw 5.6 Osaka earthquake is from the Japan Meteorological Agency (JMA) moment tensor catalogue. The red lines are active faults derived from the Active Fault Database of Japan by the National Institute of Advanced Industrial Science and Technology (AIST), where the Arima–Takatsuki (AT) fault zone is denoted. The dots indicate background seismicity of $M \geq 1.0$, and the yellow circles represent deep low-frequency earthquakes from October 1997 to December 2021 from the JMA seismicity catalogue. The north-south vertical cross-section is shown in the right panel. Synthetic wavefields of the M2.8 and M3.2 earthquakes are calculated in the region bounded by the dashed rectangle. The wavefields at the vertical cross-section AA' are illustrated in Supplementary Video S1 online. The top and bottom boundaries of the reflection layer that is assumed are drawn in the vertical cross-section, with the location of Reflector W between two grey parentheses noted in a previous study[14].

investigation based on DAS measurements of such a seismic structure can provide further information on the significance of reflectors and the intriguing low-frequency earthquakes that occur in deep areas of extension.

This study addresses the issue of sparse seismic wave observations via conventional approaches that deploy seismometers at each location by instead using the DAS technique along the national route in southern Kyoto, Japan (Fig. 1). Seismic waves from two small earthquakes observed at 9,788 stations via the DAS technique in 2021 show a spatially continuous distribution that cannot be obtained from observations via seismometers. Single earthquake observations have even proven to be sufficient for illuminating reflected waves, whereas previous studies needed 182 earthquakes and 128 seismic stations[13]. This information is used to investigate the reflector structure in the crust using three-dimensional full waveform simulation. This forwards approach can provide further understanding of the reflector. Finally, we discuss why such a layer exists in the lower crust near low-frequency earthquakes isolated from volcanoes and plate boundaries.

Strain-rate wavefields observed via DAS for the M2.8 and M3.2 earthquakes

During the period of DAS observation, the two observed earthquakes, M2.8 and M3.2, clearly showed reflected waves following direct S waves (Figs. 2, 3, 4 and 5) (see section Methodologies). These waves were the reflected S waves found by previous studies[12–14] via seismometers when the travel time was considered. Seismic waves from other small earthquakes with magnitudes greater than 0.4 were also observed; however, their reflected waves were not visible or widely observed over the optical cable, primarily because of their poor signal-to-noise ratios.

The M2.8 earthquake on September 18, 2021 (20:11 UT + 9), occurred almost below the middle of the optic cable at a depth of 11.7 km (Fig. 1). The focal mechanism indicated a reverse fault with a N-S strike. This event clearly showed the propagation of seismic waves on both sides of the cable (Fig. 2a). P wave arrivals at northwestern channels at distances greater than 48 km did not emerge because of low P wave amplitudes. The S wave arrivals were visible on all the channels, whereas some parts of the S wave amplitudes were clipped because of the phase cycle-skipping phenomena. Both the P and S waves were followed by surface waves at slower apparent velocities. These waves were then followed by the reflected S waves of interest that appeared at distances greater than approximately 13 km along the cable. The reflected waves were not visible at stations closer than 10 km. To clarify the arrivals of the reflected waves, we obtained the envelope waveforms at distances between 20 and 50 km and employed slant stack analysis. Figure 3 depicts the stacked envelope and the envelope corrected for geometrical spreading and coda attenuation[13]. The reflected waves were distinctly observed at approximately 9.5 s, had a duration of approximately 1 s when their amplitude exceeded 50% of the peak amplitude, and accompanied the coda decay. These waves were not aftershock waves, as wavefields for a longer time window of 60 s showed that a small aftershock was observed approximately 22 s later, and the travel time curve shapes and seismic phase features differed between them (see Supplementary Fig. S1 online). Notably, DAS could clearly record the seismic wavefields of this early aftershock, but this event was too small to obtain its hypocentre and magnitude and was not listed in the Japan Meteorological Agency (JMA) seismicity catalogue.

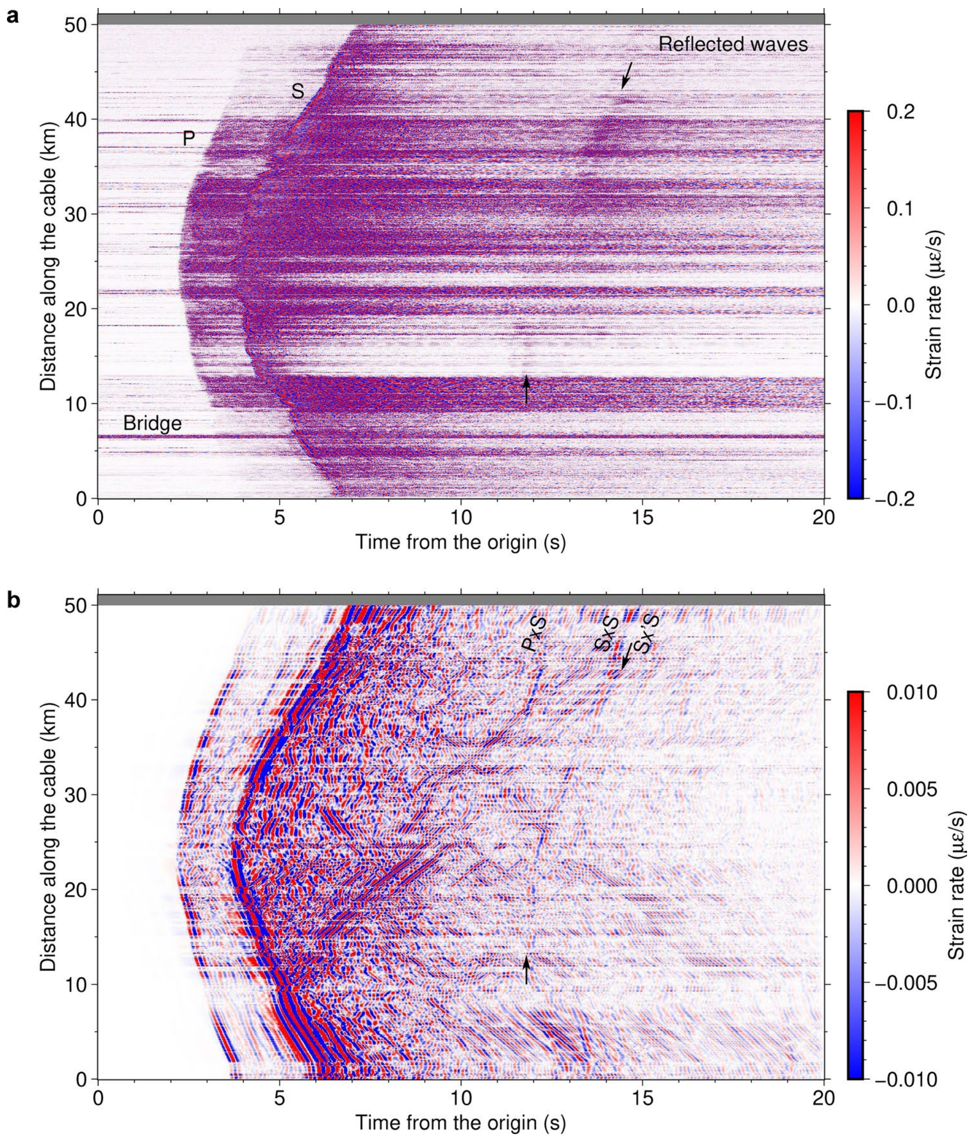

Fig. 2. Strain-rate distributions from the M2.8 earthquake. (**a**) The amplitude is the strain rate along the fibre-optic cable observed by DAS. The time sampling is reduced from 500 to 50 sps after a bandpass filter from 1 to 10 Hz. The lateral axis shows the time from the origin of the earthquake. P- and S-wavefronts are denoted. The black arrows indicate the arrivals of the reflected waves. (**b**) Numerically simulated strain rate along the cable. PxS is the P-to-S converted wave from the reflection on top of the inclined layer, SxS is the S-to-S reflection on top of the layer, and Sx'S is the S-to-S reflection on the bottom. The black arrows obtained in (a) are plotted.

We cannot locate this event; however, it should have been located close to the M2.8 earthquake, on the basis of the similarity of travel time curves. The large, narrow horizontal amplitudes, as shown in Fig. 2a, usually appear when heavy cars travel over the area or where bridges are located. Since the observed amplitudes included site amplification and coupling between the cable and ground, spatial variations in the amplitude appeared along the cable. For example, the amplitudes became relatively high at distances between 10 and 13 km. This earthquake was observed above the cable, corresponding to a distance of 17.4 km along the cable and channel number 3410, by a collocated three-component seismic sensor with a natural frequency of 2 Hz (Fig. 4). The P- and S-wave arrivals were consistent between both measurements, and the reflected S-waves were also observed at approximately 12 s in both records. Although the strain rate was approximately proportional to the acceleration, we could not directly compare these waveforms since the cable at this site strikes generally east–west along the winding road at the mountain site. The power spectra of the P wave, S wave and reflected wave significantly exceeded that of the background, particularly for low-frequency components (Fig. 4c).

The M3.2 earthquake occurred on September 11, 2021 (19:56 UT + 9), at a depth of 6.6 km and involved a strike-slip mechanism (Fig. 1). Similar to the M2.8 event, some parts of the body waves were clipped because of phase cycle-skipping phenomena (Fig. 5a). The reflected waves were vaguely observed approximately 16–17 s after the origin time, with apparent velocities faster than those of M2.8. This occurred because the M3.2 event was shallower than the M2.8 event, the reflected wave amplitude attenuated with increasing propagation

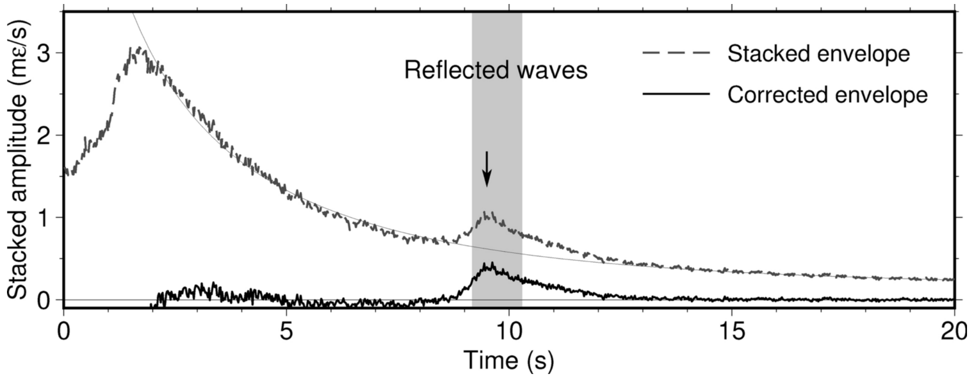

Fig. 3. Stacked envelopes of the strain-rate waveforms observed by DAS. The slant-stacked envelope using the DAS waveforms at distances between 20 and 50 km is shown as a dashed line. The thin curve is a fit to the stacked envelope, and the difference is the corrected envelope, as shown by the black solid line. The reflected waves are observed at approximately 9.5 s, as indicated by the black arrow. The wide grey bar indicates the duration of the reflected waves with amplitudes exceeding 50% of the peak amplitude.

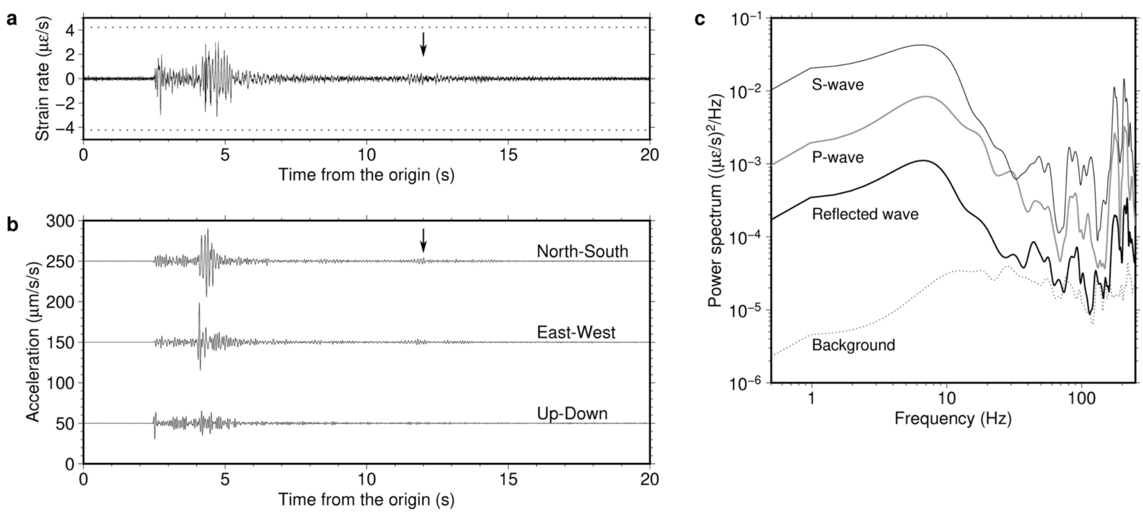

Fig. 4. Waveforms of the M2.8 earthquake. (**a**) Strain-rate waveform observed via DAS at channel 3,410. (**b**) Acceleration waveforms observed by a three-component seismometer at the corresponding station above the cable. The three traces are the north-south, east-west, and up-down components. The reflected waves are observed at approximately 12 s, as indicated by the black arrow. (**c**) Power spectra of the strain-rate waveform (**a**). The spectra of the background before P onset, P wave, S wave, and reflected wave for 2 s. The spectral amplitudes are smoothed by Parzen's spectral window with a bandwidth of 8 Hz.

distance, and the observed amplitude could not significantly overwhelm the coda wave amplitude. The reflected waves were not visible at short distances along the cable.

Note that the mechanisms of both earthquakes were consistent with the background stress field of east-west compression estimated from seismic data[15,16] and geodetic data[17].

Comparison with synthetically simulated strain-rate wavefields

Figure 2 compares the observed strain-rate field along the cable and the simulation for the M2.8 earthquake (Fig. 1), where the reflector structure in the crust is assumed for the three-dimensional full waveform simulation (see section Methodologies). For this comparison, the sensitivity of each DAS channel with respect to incoming waves needs to be considered. Although the theoretical sensitivity considering the cable geometry is derived in a simple case[18], the sensitivity examination in the present case is complicated. Therefore, we adopted the forwards numerical approach to estimate the comparison together with the sensitivity examination. Difficulties in the simulation of high-frequency waves arise when the shallow structure and the coupling between the cable and soil are unclear; therefore, we focused mainly on the arrival of visible waves. In general, the simulated amplitudes were much smaller than the observed amplitudes because we excluded the sediment structure in the simulation, which can amplify the strain rate. The arrivals of both P and S waves were consistent between the DAS observations and the numerical simulations. Some surface waves with large amplitudes propagating at slow

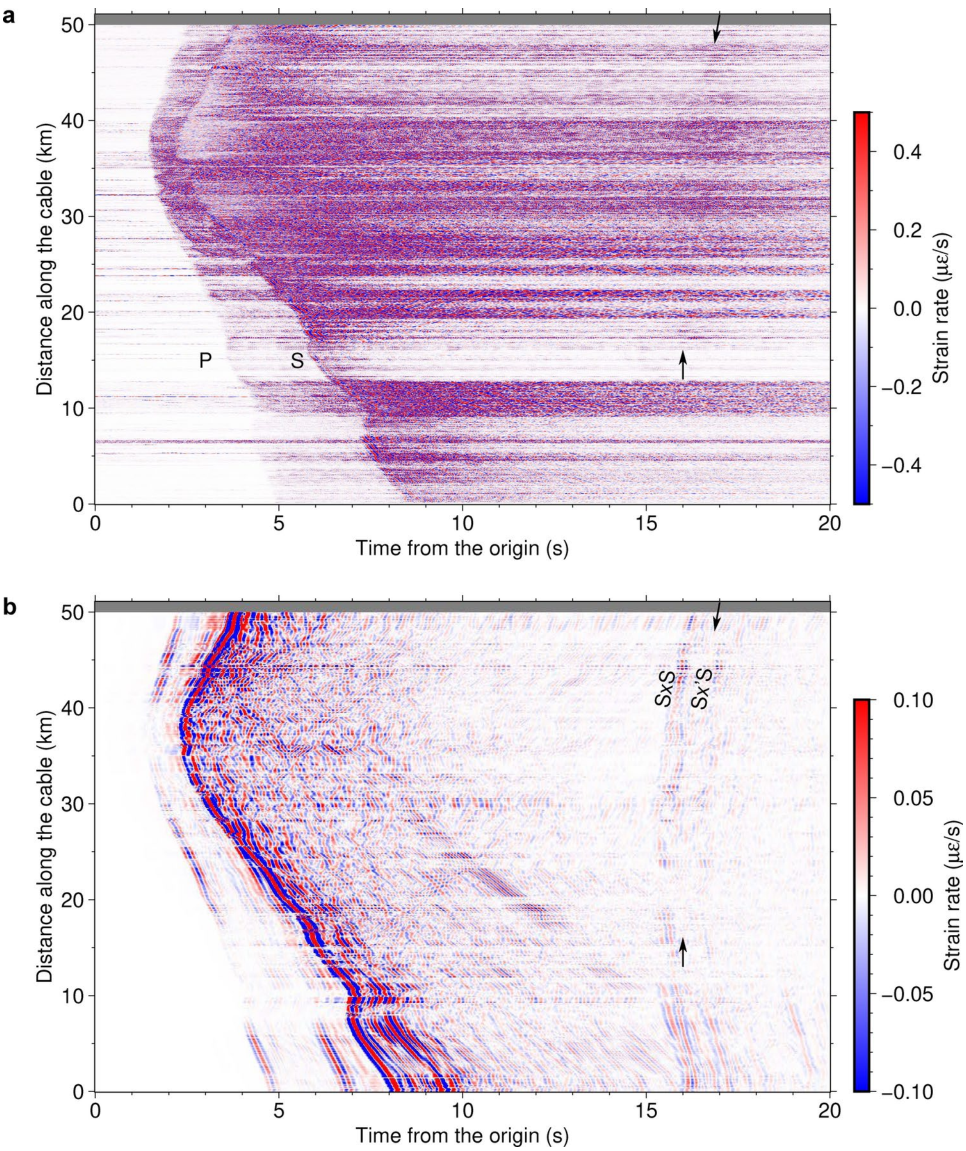

Fig. 5. Strain-rate distributions from the M3.2 earthquake. (**a**) The amplitude is the strain rate along the fibre-optic cable observed by DAS. The time sampling decreases from 500 to 50 sps after a bandpass filter from 1 to 10 Hz. P- and S-wavefronts are denoted. The black arrows indicate the arrivals of the reflected waves. (**b**) Numerically simulated strain rate along the cable. SxS and Sx'S are the same as those in Fig. 2b. The black arrows obtained in (**a**) are plotted.

apparent velocities appeared due to the surface topography; however, they were not explicitly distinguishable in DAS data. In other words, the simulated surface waves were not the only things visible in DAS observations.

The reflector structure assumed in the present model includes a low-velocity layer consisting of two different dip angles embedded in the lower crust; the dip angles are 15 deg and 30 deg in the deeper and shallower regions, respectively (Fig. 1). This model is appropriate on the basis of the results of exploratory wavefield simulations, which were examined to compare the arrivals of reflected S waves at a plain reflection layer for varying dip angles (see Supplementary Fig. S2 online). In the simulation (Fig. 2b), the reflected waves were observed from 11 to 16 s. PxS was the reflected S wave at the low-velocity layer and was converted from the P wave, and SxS and Sx'S were the S waves reflected at the top and bottom boundaries of the low-velocity layer, respectively (see Supplementary Video S1 online). PxS waves were not observed by DAS. SxS and Sx'S were consistent with the reflected S waves observed by DAS, whereas the reflected waves that corresponded exactly to SxS and Sx'S were not clearly observed. The arrivals of the large, reflected waves are visually shown by the picks in Fig. 2a, and they are plotted between the SxS and Sx'S arrivals in Fig. 2b. The duration of the reflected waves potentially corresponds to the thickness of the low-velocity layer. The arrival time of the SxS at distances from 13 to 30 km along the cable was approximately 12 s, where the waves were reflected at the upper part of the layer with a dip angle of 30 deg. As mentioned above, if we assumed only a 15-degree-dipping layer without this upwards bending structure, the arrival time was delayed and could not simulate the DAS observations (see Supplementary Figs.

S2 and S3 online); therefore, this bending structure was necessary to simulate the reflected S wave arrivals. This low-velocity structure was located within the region referred to as Reflector W in a previous study[14] (Fig. 1). The SxS waves at these distances had small amplitudes, which were also observed in the DAS observations; however, the source mechanism had some uncertainties, and different amplitude patterns appeared if different source mechanisms were given. The layer preferably needed to have strong impedance in the lower crust to generate large-amplitude reflected S waves. This means that it should have a low-velocity layer. A high-velocity structure cannot provide such a strong contrast unless we give velocity values for the deep Earth, which are unlikely to be present in the crust. Additionally, a layer with realistic high velocity for the upper mantle cannot even simulate visible reflected waves (see Supplementary Fig. S4 online).

In addition, for the M3.2 earthquake, the arrivals of P and S waves were consistent between the DAS measurements and the simulation, as shown in Fig. 5. In the simulation, SxS and Sx'S waves were visible, whereas PxS was unclear, mainly because of the geometrical attenuation of the incident P wave. The arrivals of reflected waves in the DAS observations from 15 to 18 s were visible between SxS and Sx'S in the simulation. As is the case for the M2.8 earthquake, we could not distinguish SxS and Sx'S waves in the reflected waves observed by DAS. Since the simulation had earlier arrivals of reflected waves than the DAS observations, the dip angle of the layer may be slightly larger than 15 deg in the deep part, or the velocity in the lower crust may be slightly slower than that in the present model. This aspect was not further examined because the reflected waves shown by DAS were not as clear as those shown for the M2.8 event. The surface waves propagating at slow velocities appeared in the simulated waveforms because of the surface topography, as shown in Fig. 2b.

In both cases, in the DAS observations, the reflected waves were not observed at southeastern stations. These results support the absence of reflectors in the corresponding region[12–14]. Therefore, the structural model indicates the existence of a thin layer with a low velocity that dips at a shallow angle below a depth of approximately 30 km and at a steeper angle above that depth in the area westwards from E135.7°. This bending structure has not been imaged in previous studies.

Discussion

Through numerical simulation, we can obtain the structure of the low-velocity layer in the lower crust from approximately N34.95° to N35.15° (Fig. 1), in the northern part of which characteristic deep low-frequency earthquakes are located. These isolated low-frequency earthquakes, as observed in this region, are likely generated by fluid movements[19]. The fluid related to low-frequency earthquakes is thought to play an important role in producing this reflector because the northern tip of the reflector reaches the source region of low-frequency earthquakes[13,14]. This concept is also supported by our model, in which low-frequency earthquakes are observed around a deeper part of the inclined layer with a dip angle of 15 deg. Although it is not clear how deep the reflector extends downwards in the lower crust, it is reasonable to deduce that deep low-frequency earthquakes can occur within or near the reflector.

The thickness of the layer is estimated to be approximately 0.5 km on the basis of the duration of the reflected waves. Since a trade-off exists between the low velocity in the layer and its thickness and since strong velocity impedance is required to produce clear reflected waves, the thickness may be on the order of 1 km. This value can be larger depending on the duration of time measurements. The layer may be heterogeneous and consists of multiple low-velocity sublayers since clear arrivals of the SxS and Sx'S phases from the top and bottom boundaries in the DAS observations are not found. The presence of multiple sublayers potentially obscures the arrivals of PxS waves by DAS measurements, accounting for the absence of the visibility of the Px'S waves, which are the P-to-S converted waves from the reflection on the bottom of the inclined layer, even in the simulation. Otherwise, the instrumental and background noise becomes too large, and the signal-to-noise ratio is too poor at these farther stations to observe PxS waves.

The layer potentially shows a concave upwards structure in the crust. The bending structure likely exists at depths between 25 and 30 km in the lower crust, as shown by reflected S waves at approximately 12 s in the M2.8 event. The simulation cannot provide evidence to determine whether this layer may extend to the surface since the shallower, southern layer does not contribute to the waveforms along the fibre-optic cable in the simulation. The Arima-Takatsuki (AT) fault zone consists of ENE-WSW dextral strike-slip subfaults in the southern part of this region (Fig. 1). Considering the structural geometries, it is possible for the layer and AT fault zone to intersect in the upper crust. It is well known that at the Arima hot spring in this region, slab-derived fluid, called Arima-type brine, is observed, even though no active volcanoes are nearby[20–23]. The fluid might come from the subducted Philippine Sea Plate because this plate subducts northwestwards beneath the Eurasian Plate, and the top depth of the slab is estimated at approximately 60 km in this region[24,25]. The reflector is a candidate path for fluid migration from the slab. The seismic tomography study[26] also discusses the path of slab-derived fluid beneath the AT fault zone; however, the reflector cannot be imaged due to limited spatial resolution.

In summary, we speculate that the reflection layer might reach the AT fault zone and might even become steeper in the shallower part if they are connected in the upper crust (Fig. 6). The fluid dehydrated from the subducted Philippine Sea Plate in the upper mantle moves upwards by buoyancy force. This fluid causes deep low-frequency earthquakes approximately 30–35 km deep in the lower crust, where a preexisting layer with a gentle dip angle crosses. This also means that low-frequency earthquakes rupture the structure in this inclined layer. The fluid then migrates within the layer, which results in a low-velocity zone and is observed as an S wave reflector. The thickness of the layer may be on the order of 1 km, on the basis of the duration of the observed reflected waves. The fluid migrating along the upwards concave layer eventually reaches the AT fault zone and flows out as hot spring water. Notably, such a bending structure is often observed as a listric fault along the back-arc regions in northeastern Japan because of the inversion tectonics of the Japanese Islands[27,28]; however, its distribution in this region is still unknown.

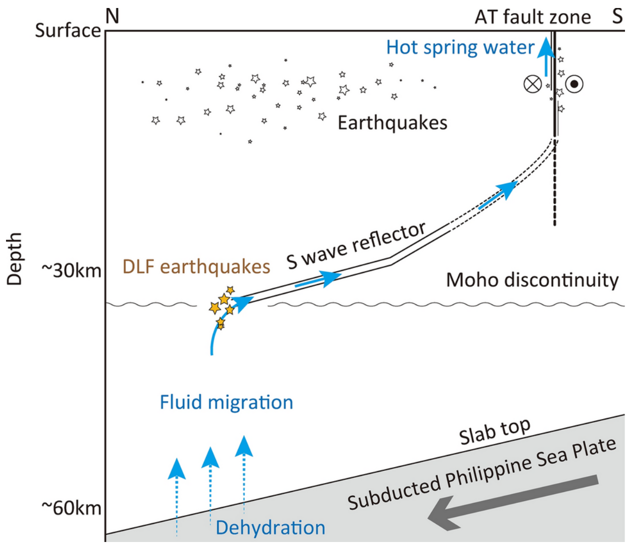

Fig. 6. Schematic of fluid migration and dehydration from the subducted slab through the preexisting layer that causes seismic wave reflections.

Methodologies

DAS data acquisition along the national route

To measure the distributed strain rate, we used a 50 km fibre-optic cable (single mode) beneath the national route in southern Kyoto, western Japan, where the cable was generally buried at depths of 0.5 m to 1 m from the surface. A DAS interrogator unit was installed at a fibre optical termination box in a Kyoto Road office building, and it continuously measured the cable for one month from August 23 to September 24, 2021, where the gauge length G was 40.8380966 m, the spatial interval was 5.1047621 m, and the sampling rate was 500 sps. The strain rates were observed at 9788 stations along the cable. The strain per sampling is obtained[29] as

$$\varepsilon = \frac{\lambda}{4\pi nG\xi}\Delta\phi \tag{1}$$

where $\Delta\phi$ is the phase change in radians, λ is the optical wavelength of 1550 nm, n is the reflection index of 1.4682, and ξ is the photoelastic scaling factor of 0.78. This value is approximately proportional to the acceleration. The amplitude was clipped in principle at ± 4.23µstrain/sec because of a phase cycle-skipping phenomenon.

The cable locations, including the altitudes, were determined from cable layout drawings (Fig. 1). Some corresponding cable channels were manually located by tapping tests at the surface and identifying bridge oscillations with higher signals than road oscillations. All other channels were located using linear interpolation. There may be spatial inconsistencies between the estimated channel location and the actual channel location, but the difference may be within tens of metres, which would not affect our results.

Three-dimensional full waveform simulation

We simulate DAS observations through a three-dimensional full waveform simulation using OpenSWPC software[30]. We modify the structure in Japan given by the JIVSM[31,32] with exponential-type random heterogeneity, with a velocity fluctuation of 1% and a characteristic scale of 0.2 km. We exclude sediment structures to stabilise the simulation near the surface. The spatial grid size is 0.02 km in the horizontal and vertical directions, and the time step is 1 ms. The computational region has an area of 18 km × 44 km and extends to a depth of 35 km (Fig. 1). An absorbing boundary condition from the auxiliary differential equation at the boundaries is given. According to the results of previous studies[13,14], a north-dipping low-velocity layer is embedded in the crust. The layer bends at a depth of 28.4 km at N34.98°, where the upper boundary dips at 15 deg and 30 deg in the northern deep area and southern shallow areas, respectively, which has not been considered in previous studies. The lower boundary is set 0.5 km below the upper boundary. The layer has a strong impedance in the lower crust due to the low-velocity layer; the density $\rho = 2.15$ g/cm^3, P wave velocity $V_P = 2.40$ km/s, S wave velocity $V_S = 1.00$ km/s, P wave attenuation factor $Q_P = 340$, and S wave attenuation factor $Q_S = 200$, which are usually used in the shallow part of the structure[30,31], whereas in the lower crust, $\rho = 2.80$ g/cm^3, $V_P = 6.40$ km/s, $V_S = 3.80$ km/s, $Q_P = 680$, and $Q_S = 400$. Supplementary Fig. S3 online shows the case considering the inclined layer with high velocity for the upper mantle, where the upper boundary is the same as for the case of the low-velocity layer, but the bottom layer is set 2.0 km below the upper boundary considering the duration of the reflected wave; $\rho = 3.20$ g/cm^3, $V_P = 7.50$ km/s, $V_S = 4.50$ km/s, $Q_P = 850$, and $Q_S = 500$; however, the amplitudes of the reflected waves are invisibly small at the same amplitude scale.

Data availability

The original dataset observed by the DAS interrogator is available from the corresponding author upon request with the permission of the Kyoto Road office that maintains the fibre-optic cable used in this study. The JMA seismicity catalogue is available at https://www.data.jma.go.jp/eqev/data/bulletin/index_e.html. The Active Fault Database of Japan by AIST[33] is available at https://gbank.gsj.jp/activefault/index_e_gmap.html. OpenSWPC is an open-source code[30] available at http://github.com/takuto-maeda/OpenSWPC. The structural model JIVSM[31] is available at https://www.jishin.go.jp/evaluation/seismic_hazard_%20map/lpshm/12_choshuki_dat/.

Received: 15 September 2023; Accepted: 18 October 2024
Published online: 28 October 2024

References

1. Li, Y., Karrenbach, M. & Ajo-Franklin, J. B. *Distributed acoustic sensing in geophysics: Methods and applications* (Wiley, 2021).
2. Lindsey, N. J., Dawe, T. C. & Ajo-Franklin, J. B. Illuminating seafloor faults and ocean dynamics with dark fiber distributed acoustic sensing. *Science* **366**, 1103–1107 (2019).
3. Lindsey, N. J., Rademacher, H. & Ajo-Franklin, B. J. On the broadband instrument response of fiber-optic DAS arrays. *J. Geophys. Res. Solid Earth*. https://doi.org/10.1029/2019JB018145 (2020).
4. Li, Z. et al. Rapid response to the 2019 Ridgecrest earthquake with distributed acoustic sensing. *AGU Adv.* https://doi.org/10.1029/2021AV000395 (2021).
5. Nishimura, T. et al. Source location of volcanic earthquakes and subsurface characterization using fiber-optic cable and distributed acoustic sensing system. *Sci. Rep.* **11**, 6319. https://doi.org/10.1038/s41598-021-85621-8 (2021).
6. Williams, E. F. et al. Distributed sensing of microseisms and teleseisms with submarine dark fibers. *Nat. Commun.* **10**, 5778. https://doi.org/10.1038/s41467-019-13262-7 (2019).
7. Yu, C., Zhan, Z., Lindsey, N. J., Ajo-Franklin, J. B. & Robertson, M. The potential of DAS in teleseismic studies: Insights from the Goldstone experiment. *Geophys. Res. Lett.* **46**, 1320–1328 (2019).
8. Ide, S., Araki, E. & Matsumoto, H. Very broadband strain-rate measurements along a submarine fiber-optic cable off Cape Muroto, Nankai subduction zone. *Japan. Earth Planets Space* **73**, 63. https://doi.org/10.1186/s40623-021-01385-5 (2021).
9. Fukushima, S. et al. Detailed S-wave velocity structure of sediment and crust off Sanriku, Japan by a new analysis method for distributed acoustic sensing data using a seafloor cable and seismic interferometry. *Earth Planets Space* **74**, 92. https://doi.org/10.1186/s40623-022-01652-z (2022).
10. Kato, A. & Ueda, T. Source fault model of the 2018 Mw 56 northern Osaka earthquake, Japan, inferred from the aftershock sequence. *Earth Planets Space* **71**, 11. https://doi.org/10.1186/s40623-019-0995-9 (2019).
11. Hallo, M., Opršal, I., Asano, K. & Gallovič, F. Seismotectonics of the 2018 northern Osaka M61 earthquake and its aftershocks: Joint movements on strike-slip and reverse faults in inland Japan. *Earth Planets Space* **71**, 34. https://doi.org/10.1186/s40623-019-1016-8 (2019).
12. Katao, H. Seismicity in Tamba region. *Chikyu Mon.* **38**, 42–49 (2002) ((**in Japanese**)).
13. Aoki, S. et al. Three-dimensional distribution of S wave reflectors in the northern Kinki district, southwestern Japan. *Earth Planets Space* **68**, 107. https://doi.org/10.1186/s40623-016-0468-3 (2016).
14. Katoh, S. et al. The relationship between S-wave reflectors and deep low-frequency earthquakes in the northern Kinki district, southwestern Japan. *Earth Planets Space* **70**, 149. https://doi.org/10.1186/s40623-018-0921-6 (2018).
15. Terakawa, T. & Matsu'ura, M. The 3-D tectonic stress fields in and around Japan inverted from centroid moment tensor data of seismic events. *Tectonics* **29**, TC6008 (2010).
16. Uchide, T., Shiina, T. & Imanishi, K. Stress map of Japan: Detailed nationwide crustal stress field inferred from focal mechanism solutions of numerous microearthquakes. *J. Geophys. Res.* **127**, e20220JB24036 (2022).
17. Okazaki, T., Fukahata, Y. & Nishimura, T. Consistent estimation of strain-rate fields from GNSS velocity data using basis function expansion with ABIC. *Earth Planets Space* **73**, 153. https://doi.org/10.1186/s40623-021-01474-5 (2021).
18. Martin, E. R., Lindsey, N. J., Ajo-Franklin, J. B. & Biondi, B. L. Introduction to interferometry of fiber-optic strain measurements. In *Distributed Acoustic sensing in geophysics* (eds Li, Y. et al.) 113–129 (Wiley, 2021).
19. Aso, N., Ohta, K. & Ide, S. Tectonic, volcanic, and semi-volcanic deep low-frequency earthquakes in western Japan. *Tectonophys.* **600**, 27–40 (2013).
20. Matsubaya, O., Sakai, H., Kusachi, I. & Satake, H. Hydrogen and oxygen isotopic ratios and major element chemistry of Japanese thermal water systems. *Geochem. J.* **7**, 123–151 (1973).
21. Morikawa, N. et al. Estimation of groundwater residence time in a geologically active region by coupling ^{4}He concentration with helium isotopic ratios. *Geophys. Res. Lett.* **32**, L02406 (2005).
22. Kusuda, C., Iwamori, H., Nakamura, H., Kazahaya, K. & Morikawa, N. Arima hot spring waters as a deep-seated brine from subducting slab. *Earth Planet Space* **66**, 119. https://doi.org/10.1186/1880-5981-66-119 (2014).
23. Iwamori, H., Nakamura, H., Chang, Q., Morikawa, N. & Haraguchi, S. Multivariate statistical analyses of rare earth element compositions of spring waters from the Arima and Kii areas Southwest Japan. *Geochem. J.* **54**, 165–182 (2020).
24. Ueno, T., Shibutani, T. & Ito, K. Configuration of the continental Moho and Philippine Sea slab in southwest Japan derived from receiver function analysis: Relation to subcrustal earthquakes. *Bull. Seism. Soc. Am.* **98**, 2416–2427 (2008).
25. Hirose, F., Nakajima, J. & Hasegawa, A. Three-dimensional seismic velocity structure and configuration of the Philippine Sea slab in southwestern Japan estimated by double-difference tomography. *J Geophys Res.* **113**, B09315 (2008).
26. Nakajima, J. The Wakayama earthquake swarm in Japan. *Earth Planets Space* **75**, 48. https://doi.org/10.1186/s40623-023-01807-6 (2023).
27. Sato, H. The relationship between Late Cenozoic tectonic events and stress field and basin development in northeast Japan. *J. Geophys. Res.* **99**, 22261–22274 (1994).
28. Okamura, Y., Watanabe, M., Morijiri, R. & Satoh, M. Rifting and basin inversion in the eastern margin of the Japan Sea. *Island Arc* **4**, 166–181 (1995).
29. Measuring Sensor Performance – DAS Parameter Definitions and Tests (SEAFOM-MSP-02), https://seafom.com/?mdocs-file=1270 (2018).
30. Maeda, T., Takemura, S. & Furumura, T. OpenSWPC: an open-source integrated parallel simulation code for modeling seismic wave propagation in 3D heterogeneous viscoelastic media. *Earth Planets Space* **69**, 102. https://doi.org/10.1186/s40623-017-0687-2 (2017).
31. Koketsu, K., Miyake, H. & Suzuki, H. Japan Integrated Velocity Structure Model Version 1. *Proc. 15th World Conf. Earthq. Eng.*, 1773 (2012).
32. Earthquake Research Committee, The Headquarters for Earthquake Research Promotion. Procedures to build a subsurface velocity structure model, https://www.jishin.go.jp/main/chousa/17apr_chikakozo/model_concept-e.pdf (2022).
33. National Institute of Advanced Industrial Science and Technology. Active Fault Database of Japan, February 28, 2012 version. Research Information Database DB095. https://gbank.gsj.jp/activefault/index_e_gmap.html (2012).

34. Wessel, P. et al. The generic mapping tools version 6. *Geochem. Geophys, Geosys.* **20**, 5556–5564. https://doi.org/10.1029/2019GC008515 (2019).

Acknowledgements
This work was supported by JSPS KAKENHI Grant Numbers JP21K18748, JP22H05306, the Disaster Prevention Research Institute's collaborative research program 2021A-06, and partly by the Ministry of Education, Culture, Sports, Science and Technology (MEXT) of Japan, under its The Second Earthquake and Volcano Hazards Observation and Research Program (Earthquake and Volcano Hazard Reduction Research). The numerical waveforms were simulated by using the computer systems of the Earthquake and Volcano Information Center of the Earthquake Research Institute (ERI), University of Tokyo, Japan. Figures 12, 3, 4 and 5 and Supplementary Figs S1-S4 were generated using GMT[34]. Discussions with T. Tsuji, H. Nakahara, K. Emoto, and Y. Iio helped develop this study.

Author contributions
M.M. acquired and analysed the dataset and wrote the manuscript.

Declarations

Competing interests
The authors declare no competing interests.

Additional information
Supplementary Information The online version contains supplementary material available at https://doi.org/10.1038/s41598-024-77024-2.

Correspondence and requests for materials should be addressed to M.M.

Reprints and permissions information is available at www.nature.com/reprints.

Publisher's note Springer Nature remains neutral with regard to jurisdictional claims in published maps and institutional affiliations.